Photo-induced terahertz near-field dynamics of graphene/InAs heterostructures

ZIHENG YAO,[1,8] VYACHESLAV SEMENENKO,[2,8] JIAWEI ZHANG,[1] SCOTT MILLS,[1] XIAOGUANG ZHAO,[3] XINZHONG CHEN,[1] HAI HU,[4] RYAN MESCALL,[1] THOMAS CIAVATTI,[1] STEPHEN MARCH,[5] SETH R. BANK,[5] TIGER H. TAO,[6] XIN ZHANG,[3] VASILI PEREBEINOS,[7,2] QING DAI,[4] XU DU,[1,9] AND MENGKUN LIU[1,10]

[1]*Department of Physics and Astronomy, Stony Brook University, Stony Brook, New York 11794, USA*
[2]*Skolkovo Institute of Science and Technology, Skolkovo, Moscow Region 143026, Russia*
[3]*Department of Mechanical Engineering, Boston University, Boston, MA 02215, USA*
[4]*Nanophotonics Research Division, CAS Center for Excellence in Nanoscience, National Center for Nanoscience and Technology, Beijing 100190, China*
[5]*Electrical and Computer Engineering, The University of Texas at Austin, Austin, TX 78758, USA*
[6]*State Key Laboratory of Transducer Technology, Shanghai Institute of Microsystem and Information Technology, Chinese Academy of Sciences, Shanghai 200050, China*
[7]*Department of Electrical Engineering, University at Buffalo, The State University of New York, Buffalo, NY 14260, USA*
[8]*These authors contributed equally*
[9]*xu.du@stonybrook.edu*
[10]*mengkun.liu@stonybrook.edu*

Abstract: In this letter, we report optical pump terahertz (THz) near-field probe (n-OPTP) and optical pump THz near-field emission (n-OPTE) experiments of graphene/InAs heterostructures. Near-field imaging contrasts between graphene and InAs using these newly developed techniques as well as spectrally integrated THz nano-imaging (THz s-SNOM) are systematically studied. We demonstrate that in the near-field regime ($\lambda / 6000$), a single layer of graphene is transparent to near-IR (800 nm) optical excitation and completely "screens" the photo-induced far-infrared (THz) dynamics in its substrate (InAs). Our work reveals unique frequency-selective ultrafast dynamics probed at the near field. It also provides strong evidence that n-OPTE nanoscopy yields contrast that distinguishes single-layer graphene from its substrate.

Introduction

The implementation of scattering-type scanning near-field optical microscopy at THz frequencies (THz-s-SNOM) with sub 100 nm spatial resolution was first demonstrated over fifteen years ago [1,2]. Recent developments have revealed its powerful capabilities for performing nano-spectroscopies without artefacts [3], probing the local carrier density in semiconductors with ultra-sensitivity [4,5] and imaging phase transitions of strongly correlated materials at elevated temperatures [6]. With recent developments in ultrafast pulse based THz near-field techniques [6], one natural extension to the existing imaging technique is to perform nanoscopy in the ultrafast time domain, where a conventional optical-pump THz-probe scheme can be utilized using high repetition rate THz pulses as the probe [7]. This has not been extensively demonstrated before in the 0.2-2 THz frequency range [8].

Another newly developed branch of the THz near-field imaging techniques which receives a significant amount of attention is n-OPTE nanoscopy. This technique was recently demonstrated using InAs as the THz near-field emitter, promising THz imaging with a < 50 nm spatial resolution [9]. This THz emission nanoscopy is potentially very powerful for

probing the local far-infrared properties of nanomaterials on select substrates and provides an interesting frontier for future research on THz emission dynamics in novel quantum materials [10–14].

In this work, we perform optical pump terahertz (THz) near-field probe (n-OPTP) and optical pump THz near-field emission (n-OPTE) experiments on graphene/InAs heterostructures. This specific sample is chosen to illustrate the unique near-field reflection and emission phenomena at THz frequencies in these two technologically important THz materials. Specifically, graphene has been demonstrated to possess unique far-infrared behavior in the extreme subwavelength regime [15,16]. Unlike in the mid-IR frequency range where plasmon propagation can be readily measured [17–22], the high momentum coupling between the photon and electrons in THz s-SNOM yields a strong tip-sample interaction and a close-to-perfect near-field THz reflection in high mobility graphene [16]. This interesting phenomenon arises naturally when evanescent optics with high in-plane light-momentum meet the high in-plane THz conductivity of graphene. As we will further demonstrate in this work, this near-perfect THz near-field reflectivity of graphene can effectively "screen out" the pump-induced carrier dynamics in its InAs substrate while graphene remains "transparent" to the optically induced THz emission from beneath.

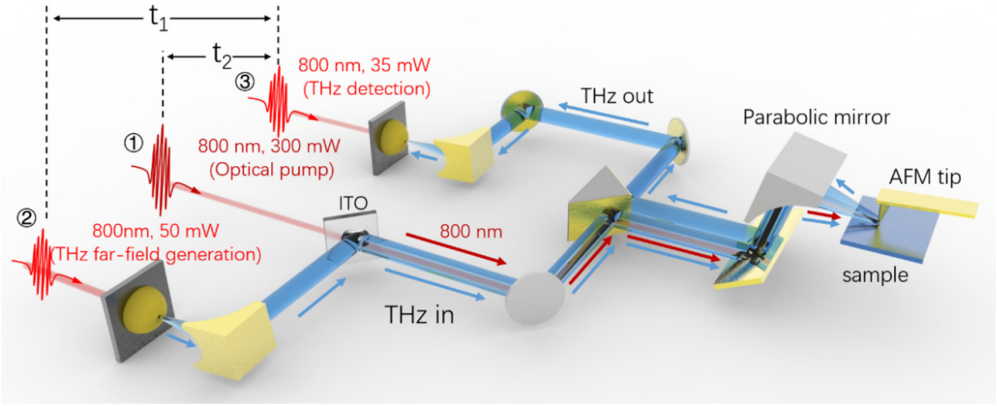

Fig. 1. Schematic of the near field optical-pump THz-probe (n-OPTP) setup, equally capable of performing optical pump near-field THz emission (n-OPTE) experiments. ①: 800 nm, 300 mW pump pulses pass through the ITO then go through the center of, while parallel to, the THz beam ②. Optical pump ① and THz probe ② are focused onto the AFM tip apex using an off-axis parabolic mirror. ③: THz gate (detection) beam. Tip scattered THz signals can be mapped out in the time domain by modifying the arrival time of THz gate beam ③ to the THz photoconductive antenna detector, thus changing the delay between ② and ③ (t_1). Changing the delay between ① and ③ (t_2) by modifying arrival time of pump pulse ① probes the photo-excited ultrafast dynamics of the sample (see main text), where in this work, t_1 is fixed at the peak position of the scattered THz electric field while t_2 is varied to yield n-OPTE (with THz probe ② blocked) and n-OPTP (with THz probe ② unblocked) measurements.

Methods

In Fig. 1, we illustrate our home-built THz near-field system based on a commercial AFM (NT-MDT NTEGRA Lite). The 800 nm pulses are generated using a 35 fs, 78 MHz Ti-sapphire oscillator (Spectra-Physics MaiTai SP). We split the 800 nm beam into three separate optical paths: the optical pump beam, the THz probe generation beam and the THz gate (detection) beam (①, ②, ③ respectively, as shown in Fig. 1), which is the same as a typical far-field OPTP setup. The THz pulses are generated and detected through a pair of THz photoconductive antennas (PCA, TeTechS inc.). To perform near-field THz measurement and achieve ~50 nm spatial resolution, the THz beam is focused onto the AFM tip with a diffraction-limited spot using a 50.8 mm diameter parabolic mirror with a focal length of 38.1 mm. The back scattered THz light from the tip is collected by the same

parabolic mirror and then directed into another PCA detector following a separate beam path. By modifying the arrival time of gate beam to the PCA detector, we are able to adjust the time delay between the 800 nm gate beam and THz beam (t_1), allowing us to effectively map the THz electric field in the time-domain (THz time-domain spectroscopy, THz-TDS). When performing the pump-probe measurement, t_1 is fixed at the peak position of the THz pulse and the time delay between the pump and the gate beam (t_2) is varied by modifying the arrival time of the pump pulse. By convention, in the following discussions of n-OPTP, time zero is set to when the optical pump pulse and the peak of THz probe pulse overlay one another.

To yield genuine near-field signal from the tip-sample interaction and eliminate the far field backgrounds, we demodulate the scattered THz signal at the second harmonic of the tip tapping frequency. The signal-to-noise ratio of the near-field signal S_2 is approximately 14:1, using an integration time per pixel of 100 ms. The graphene samples are exfoliated onto PDMS (polydimethylsiloxane) and then transferred onto 2 μm InAs thin film grown on 500 μm GaAs substrate. The InAs layer was grown via molecular beam epitaxy (MBE) and Si-doped to ~10^{17} cm^{-3} [23].

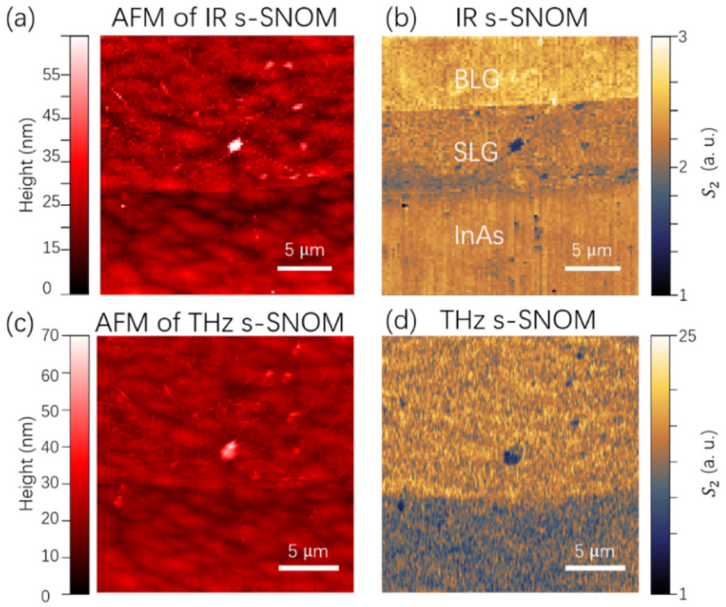

Fig. 2. IR and THz s-SNOM of a graphene/InAs heterostructure. (a): AFM topography using IR near-field scanning system. (b): IR s-SNOM obtained simultaneously with (a). The bare InAs substrate, single layer graphene (SLG) and bilayer graphene (BLG) are easily distinguishable. The wavelength of the IR light is ~10.8 μm. (c): AFM topography using THz near-field system on the same sample area with (a). (d): THz s-SNOM image obtained simultaneously with (c). The regions covered by graphene, regardless of number of layers, show almost identical near-field (S_2) contrast.

Results

Prior to the discussion of the ultrafast dynamic responses, we first compare the THz s-SNOM imaging with the IR s-SNOM imaging of a graphene/InAs heterostructure. The static THz near-field imaging is done by blocking beam ① and allowing beams ② and ③ to operate. In Fig. 2, we show the AFM topography (left) and near-field images (right) of the same sample using mid-IR (top row) and THz (bottom row) s-SNOM without the 800 nm pump. (The near-field IR imaging is performed using a separate system with a CO_2 laser at ~10.8 μm [24,25].) The AFM topography mappings in both systems yield similar results which verifies that the location and quality of the sample is maintained between measurements. For IR near-field

imaging, the difference between the InAs substrate and graphene is relatively small, while the contrast between the different number of layers of graphene is evident; one can easily distinguish single layer graphene (SLG) and bilayer graphene (BLG). In comparison, for THz near-field imaging, there is a strong contrast between the bare InAs substrate and the graphene, while the single layer and bilayer graphene are indistinguishable. We have previously reported on the similarity of THz near field signals among different layers of graphene and its close to unity signal level [16]. We note that for high quality graphene samples with typical doping at ambient environment conditions such as ours, it has been documented that the single layer and bilayer graphene are indistinguishable [26]. However, it is possible that when the Fermi level is much closer to the Dirac point (within several meV), the differences between single layer and bilayer graphene can still be resolved with THz near-field imaging. The mobility and asymmetry of electrons or holes may also contribute to this distinguishability, providing an interesting subject for future studies.

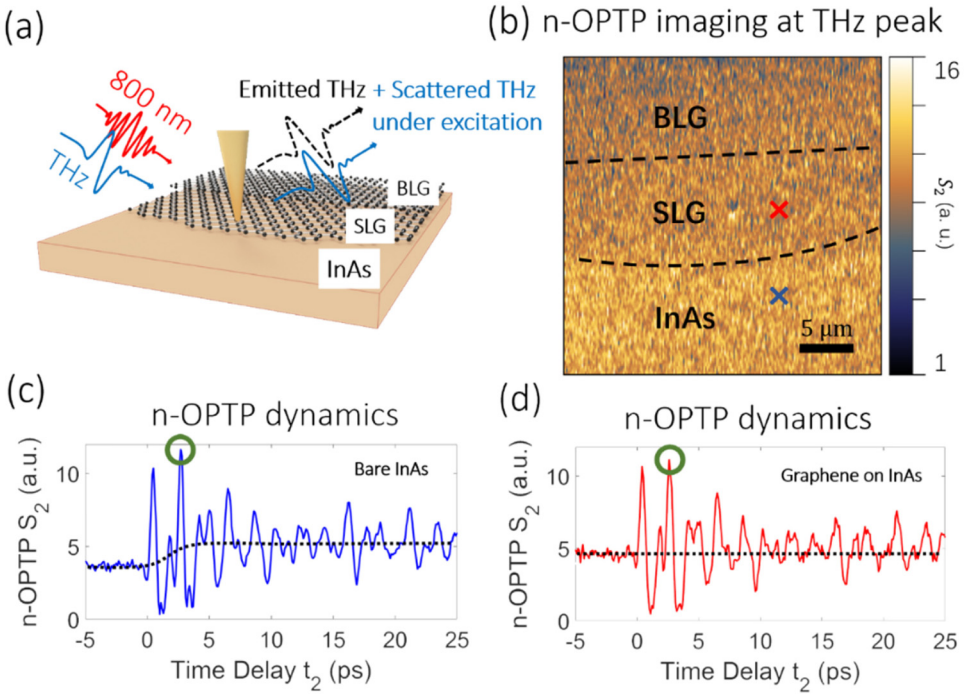

Fig. 3. Near-field optical pump THz probe (n-OPTP) measurements of a graphene/InAs heterostructure. (a): Schematic of the experimental setup. SLG: single layer graphene. BLG: bilayer graphene. The tip-scattered signal includes 800 nm pump induced THz emission and near-field reflection of the incident THz pulses under photo-excitation. (b): The n-OPTP imaging of the InAs-SLG/InAs boundary at the same region as shown in Fig. 2. The time delay t_2 between the gate beam and pump is fixed at when the THz signal reaches its maximum value (indicated by the green circles in panels (c) and (d)). Scale bar: 5 μm. (c): n-OPTP dynamics of bare InAs substrate taken with the tip located at the blue cross in (b). The dotted black line is a guide to the eye, showing the rise in the baseline of THz near-field reflectivity after InAs is pumped. (d): n-OPTP dynamics of SLG/InAs taken with the tip located at the red cross in (b). The dotted line shows that there is no notable change for the baseline of THz reflection signal before and after the pumping of SLG/InAs.

Next, we discuss the n-OPTP measurements, which are the main results of this letter. Figure 3(a) illustrates the experimental setup where the optical pump and THz probe are both present. Therefore, the photo-induced n-OPTP dynamics contain contributions from both the THz emission and the THz near-field scattered signal. In contrast to the THz near-field imaging without the pump (Fig. 2(d)), near-field OPTP imaging reveals slightly higher

signals from the bare InAs than that from single-layer graphene/InAs (SLG/InAs) (Fig. 3(b), with t_2 fixed at the peak of THz field). This small signal contrast will be discussed later. In Figs. 3(c) and 3(d), we demonstrate the n-OPTP dynamics of the bare InAs and SLG/InAs, respectively. In bare InAs, with 800 nm optical excitation, both near-field THz generation and photo-induced ultrafast carrier dynamics are present. The emitted near-field THz signal is the oscillatory part of the curve in Fig. 3(c), while the pump-induced carrier dynamics in InAs cause the rising baseline indicated by the dotted black curve. Oppositely, for SLG/InAs the rise of the baseline does not appear (indicated by the dotted black curve in Fig. 3(d)), suggesting that the signal from the carrier dynamics, here the change of near-field reflectivity in THz range, in InAs is effectively screened out by graphene. Since the THz near-field signal in this n-OPTP measurement includes both the near-field THz emission and the THz scattering, extra steps must be executed to identify the contributions of the two different dynamics.

With the incident THz beam ② blocked, we record only the THz emission signal via n-OPTE experiments. The experiment is schematically shown in Fig. 4(a). It is clear that the near-field THz emission microscopy yields very small contrast between bare InAs and SLG/InAs (Fig. 4(b)). The emission signal is taken with t_2 at the THz peak (green circle in Figs. 4(c) and 4(d)). Upon comparison of the n-OPTE dynamics between Figs. 4(c) and 4(d), it becomes evident that InAs shows comparable THz near-field emission signal with or without the graphene coverage. The bare InAs is only slightly (<10%) higher. This suggests that the optically generated THz emission from the InAs substrate is not blocked by SLG. Moreover, this small contrast between graphene and InAs in Fig. 4(b) proves that the THz near-field emission nanoscopy works with an optical contrast that distinguishes a single atomic layer. In addition, since the incident THz probe light is absent, neither SLG nor InAs shows a rising "baseline" in n-OPTE experiments (Figs. 4(c) and 4(d)). This suggests that the rising baseline in the n-OPTP experiment (Fig. 3(c)) indeed results from pump induced carrier dynamics in InAs, which manifests itself as an increase of THz near-field reflectivity following optical excitation. Such photoinduced THz dynamics in InAs can be effectively screened by a single layer of graphene, which agrees with our previous observations: with high light momentum, graphene shows close to unity reflectivity at the THz frequencies despite the change of optical properties in the substrate [16].

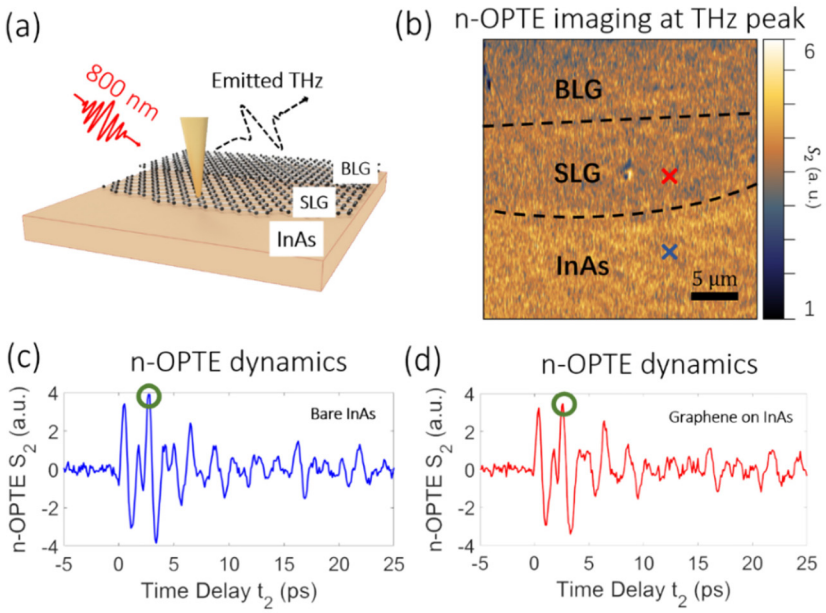

Fig. 4. (a): Schematic of the near-field optical pump THz emission (n-OPTE) experiment. The tip scattered THz signal is induced by an 800 nm pump in InAs [9]. (b): n-OPTE imaging of graphene/InAs heterostructure and bare InAs substrate at the same region as in Fig. 2 and Fig. 3. t_2 is fixed at the peak position of the THz emission, indicated by the green circles in (c) and (d). (c) and (d): n-OPTE dynamics of InAs and SLG/InAs, respectively. The signals are comparable, with the peak slightly lower in the case of SLG/InAs. Graphene does not screen the THz emission from the underlying InAs substrate.

Discussion

For completeness, we also performed a rigorous calculation to understand the near field contrast at various frequencies. The details of the model are described in the Appendix, which produces similar results to the point dipole analysis [27]. The complex dielectric function of InAs and the complex 2d conductivity of graphene are used to yield simulated s-SNOM S_2 signals. The conductivity of graphene was modeled by Eq. (4) in the Appendix, as derived in [28], where a scattering rate of v = 10 meV and a temperature of T = 300 K is used. The dielectric properties of InAs were determined by the Drude formula, which is extensively used in probing semiconductors with s-SNOM technique [4,29–31]. The effect of optical pumping is modeled by the rise of carrier density N_d to ~10^{19} cm^{-3} [32]. The parameters for the Drude formula are the following: $\varepsilon_{InAs} = 14.2$, $\omega_p^2 = 4\pi e^2 N_d / \varepsilon_{\mathrm{InAs}} m_e^*$ and $\nu = e/\mu m_e^*$, where $\varepsilon_{\mathrm{InAs}}$, ω_p and v are the low-frequency dielectric permittivity of intrinsic InAs, the plasma frequency and the scattering rate, respectively. Correspondingly, $m_e^* = 0.026 m_e$ is the effective electron mass and μ = 3.5·10^3~2.5·10^4 cm^2/Vs is the mobility [23,33]. Figure 5 shows the simulation results of the S_2 signal acquired from bare InAs, as well as InAs covered by SLG with various carrier mobilities and carrier densities of InAs and Fermi energies of graphene. From the solid curves in Fig. 5, it is seen that SLG exhibits its screening properties at frequencies below about 1-2 THz (photon energy is about 4-8 meV), more or less independently from its Fermi energy. This is in agreement with the relatively simple concept of oscillation theory which states that an action on a system with a frequency below its reversed relaxation time (that equals v = 10 meV in the case of SLG) can be considered as (quasi)static.

Similar behavior of the S_2 frequency dependence occurs in the case of bare InAs (dotted curves in Fig. 5). The plasma frequency $\omega_p = \sqrt{4\pi e^2 N_d / \varepsilon_{\mathrm{InAs}} m_e^*}$ in InAs separates the low-frequency case when InAs can be considered as perfect conductor and high-frequency case when InAs can be considered as intrinsic [4]. The width of transmission region $\Delta\omega$ is about ν, where ν is electron scattering rate in InAs. From a qualitative point of view, the dependencies are in agreement with the S_2 contrasts between bare InAs and InAs covered by SLG or BLG obtained in the experiments. Approximately, BLG can be considered as SLG under the same conditions, but with twice the conductivity (see Appendix). In our case, it's difficult to reproduce the specific contrasts observed in experiment due to several reasons. The first is that the exact values of the Fermi energy and of the electron scattering rate in graphene are unknown. The second is that we are probing the surface depletion layer of InAs where the carrier density is effectively reduced [34]. The third is that the tip enhanced THz field effectively reduces the carrier mobility [23]. Simulations that can achieve exact replication of experimental results demands further research work.

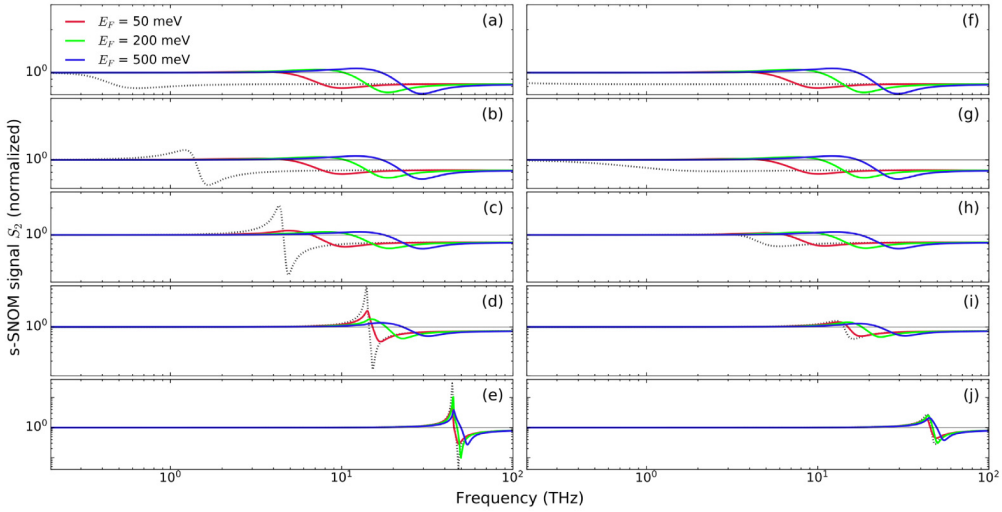

Fig. 5. Simulated s-SNOM S_2 signals vs incident light frequency (ω) for different carrier mobilities and carrier densities in InAs, and different Fermi energies in graphene. Dotted curves are for bare InAs and solid curves for InAs covered by SLG. The same columns are for the same carrier mobility in InAs and the same rows are for the same carrier density in InAs. (a)-(e): $\mu_{\mathrm{InAs}} = 2.5\times10^4$ cm^2/Vs. (f)-(j), $\mu_{\mathrm{InAs}} = 3.5\times10^3$ cm^2/Vs. (a) and (f): InAs carrier density $N_d = 10^{15}$cm^{-3}. (b) and (g): $N_d = 10^{16}$ cm^{-3}. (c) and (h): $N_d = 10^{17}$ cm^{-3}. (d) and (i): $N_d = 10^{18}$ cm^{-3}. (e) and (j): $N_d = 10^{19}$ cm^{-3}. Note that both axes are in logarithmic scale. The y-axes appear in different scale for different rows. All the signals are normalized to those of bare gold under the same conditions. The dielectric permittivity of the gold reference was calculated using the Drude formula with a plasma frequency of ω_p = 8.45 eV and a scattering time of ν^{-1} = 14 fs [35].

Conclusion

From the coherent study of the pump induced THz near-field dynamics, we conclude that a single layer of graphene is a near-perfect THz near-field "scatterer". It can couple the THz field from above or below, incident or generated, to the AFM tip and lead to near-unity near-field scattering dynamics. Concurrently, graphene serves as a near-perfect shield to the dynamic changes of the physical properties (e.g. THz conductivity) of the substrate. Combined with the InAs-based THz near-field emission microscopy techniques, our study provides a useful route for manipulating the ultrafast far-infrared responses of low dimensional materials at the nanoscale. Future studies can investigate the gate control of the

THz pump probe or emission dynamics of low dimensional materials with confined geometry, preferably at cryogenic temperatures.

Appendix

To simulate the s-SNOM signal in the experiment, we consider the tip as an infinite cylinder of radius *a*=30 nm oriented along the *y*-axis and located at a varying height *h(t)* above the sensed surface (located in *XY* plane). The electric field measured at the cylinder's center is the superposition of the incident field $\mathbf{E}^{inc}(t)=\mathbf{E}_0^{inc}e^{i\omega t}$ and the scattered field $\mathbf{E}^{sc}(t)=\mathbf{E}_0^{sc}e^{i\omega t}$, generated by the dipole moment $\mathbf{p}(t)=\mathbf{p}_0e^{i\omega t}$ *per unit length* in the cylinder. Here we consider $\mathbf{E}_0^{inc}$ as the vector directed along the *z*-axis: $\mathbf{E}_0^{inc}=(0,0,E_0)$, $\mathbf{E}_0^{sc}=(0,0,E_0^{sc})$ and $\mathbf{p}_0=(0,0,p_0)$ are the vectors in *XZ* plane. Taking into account that $c/\omega \gg h,\lambda_p$, where λ_p is the wavelength of the plasmons excited in the graphene, we can find the electric field generated by the dipole, neglecting the radiation compound, as:

$$\mathbf{e}(\mathbf{r},t)=\frac{4\mathbf{p}(t)\cdot[\mathbf{r}_{XZ}-\mathbf{h}_{XZ}]}{(\mathbf{r}_{XZ}-\mathbf{h}_{XZ})^4}(\mathbf{r}_{XZ}-\mathbf{h}_{XZ})-\frac{2\mathbf{p}(t)}{(\mathbf{r}_{XZ}-\mathbf{h}_{XZ})^2} \tag{1}$$

where the "*XZ*" subscript represents the projection operation to the *XZ* plane:

$$\mathbf{v}_{XZ}=\mathbf{v}-\left(\mathbf{v}\cdot\hat{\mathbf{y}}\right)\mathbf{v},\hat{\mathbf{y}}=(0,1,0)$$

$\mathbf{r}$ is the coordinate vector and $\mathbf{h}=(0,0,h)$ is the radius vector of the dipole position. For better convergence and possibility to apply the Fourier method to solve Maxwell equations, we consider a periodic geometry along the *x*-direction with a period of $d \gg h,\lambda_p,L_p$, where L_p is the graphene plasmon propagation length. To allow the excited electric field to satisfy the Poisson equation, we consider periodic dipoles that give the field the expression:

$$\mathbf{E}(\mathbf{r},t)=\sum_{k=-M}^{M}\mathbf{e}(\mathbf{r}-k\cdot\mathbf{d},t)$$

where $\mathbf{d}=(0,0,d)$ is the periodic translation vector and $M\to\infty$ is the number of neighbors (at one side) taken into account. In this case, at the investigated surface (at $z = 0$) we represent the component of the excited electric field parallel to the surface $E_x(x,t)$ and the component of the electric displacement vector normal to the surface $D_z(x,t)$ as the following Fourier series:

$$E_x(x,t)=e^{i\omega t}\sum_{j=-N}^{N}\varepsilon_{0j}e^{-iq_jx},\ D_z(x,t)=e^{i\omega t}\sum_{j=-N}^{N}\Delta_{0j}e^{-iq_jx} \tag{2}$$

where $q_j=b_0j$ and $b_0=2\pi/d$ are wavevectors of the *j*th and the first harmonics, respectively. $N\to\infty$ is the highest Fourier harmonic taken into account. The reflected electric field can be represented as

$$E^{(0)}=\sum_{j=-N}^{N}a_j\begin{bmatrix}i\kappa_{0j}\\0\\q_j\end{bmatrix}\exp\left(i\omega t-iq_jx-\kappa_{0j}z\right) \tag{3}$$

$$\kappa_{0j}=\sqrt{q_j^2+\varepsilon_0\omega^2/c^2}$$

where a_j are unknown amplitudes of Fourier harmonics and ε_0 is the dielectric permittivity of the media at which the tip is located.

The wafer can be made of n+1 layers of materials with different dielectric permittivities ε_l and thicknesses h_l. We imply that the last material has an infinite thickness, $h_{n+1} = \infty$. The electric field in the medium with index l can be represented as follows:

$$\mathbf{E}^{(l)} = e^{i\omega t} \sum_{j=-N}^{N} e^{-ik_0 a_{l,j} x} \left\{ A_{l,j} \begin{bmatrix} \gamma_{l,j} \\ 0 \\ \alpha_{l,j} \end{bmatrix} e^{-ib_0 \gamma_{l,j} z} + B_{l,j} \begin{bmatrix} -\gamma_{l,j} \\ 0 \\ \alpha_{l,j} \end{bmatrix} e^{ib_0 \gamma_{l,j} (z+h_l)} \right\}$$

where $\gamma_{l,j} = \sqrt{\varepsilon_l \omega^2 / c^2 - b_0^2 \alpha_{lj}^2} / b_0$, $0 < \arg \gamma_{l,j} < \pi$, $\alpha_{l,j} = j$ and $B_{n+1,j} = 0$. In each layer the z-coordinate is counted from its interface with the medium at the upper layer. It is possible to calculate the ratio

$$\frac{D_{zj}^{(1)}}{E_{xj}^{(1)}} = \frac{\varepsilon_1 \alpha_{1,j}}{\gamma_{1,j}} \times \Xi_j$$

for each harmonic. For the case of n = 0 (tip senses semi-infinite material), the expression reduces to a trivial case because $\Xi_j = 1$.

In addition to the equations above, we enact the following additional conditions:

- Boundary conditions between the media with l = 0 and l = 1:

  $$E_x^{(0)} = E_x^{(1)}, D_z^{(0)} - D_z^{(1)} = 4\pi\sigma$$

  where σ is the distribution of the sheet density of free charges at the interface.

- Continuity equation at the interface:

  $$\frac{\partial \sigma}{\partial t} + \frac{\partial j}{\partial x} = 0$$

  where j is the sheet current density at the interface.

- Transport equation (Ohm's law in our case) for the current:

  $$j_\omega = \lambda_\omega E_{x\omega}^{(0)}$$

  where the "ω"-subscript represents the Fourier transform of a function in the time domain and λ_ω is the conductivity of the 2d-material covering the bulk material layer with dielectric permittivity ε_l. For instance, if the 2d-covering is absent, λ_ω = 0; if the 2d-material is single layer graphene, λ_ω can be calculated using the formula [28]:

  $$\lambda_\omega = \frac{e^2 k_B T}{\pi\hbar^2 (i\omega + \nu)} \left(\frac{\mu_c}{k_B T} + 2\log\left(e^{-\mu_c / k_B T} + 1 \right) \right) + \frac{e^2 (\omega - i\nu)}{i\pi\hbar^2} \int_0^\infty \frac{f_d(-E) - f_d(E)}{(\omega - i\nu)^2 - 4(E/\hbar)^2} dE \qquad (4)$$

  where μ_c is its chemical potential, ν is the electron scattering rate in it, T is the temperature, k_B is the Boltzmann's constant and $f_d(E)$ is Fermi distribution:

  $$f_d(E) = \frac{1}{1 + \exp\left[(E - \mu_c) / k_B T \right]}$$

The equations above have been widely used in similar works, for example, in verification of graphene plasmon using s-SNOM measurements [36,37].

If the 2d material is an AB-stacked bilayer of graphene, in the THz and IR frequency ranges (where the photon energy is less than ~400 meV) its conductivity can be taken to be approximately twice that of the single layer graphene. This can be checked by comparing numerical results obtained using equations 3 and 4 in [28] and the ones obtained by equations 19–21 in [38] and equations 4–6 in [39]. Note that in our case, the basis functions are $\exp\left(+i\omega t - i\mathbf{k}\cdot\mathbf{r}\right)$ with a "+" sign before $i\omega$ and Kramers-Kronig relation (equation 4 in [39]) has the opposite sign:

$$\operatorname{Im}\lambda(\omega) = +\frac{2\omega}{\pi}\int_0^\infty \frac{\operatorname{Re}\left[\lambda(\omega)-\lambda(\infty)\right]}{\omega'^2-\omega^2}\mathrm{d}\omega'$$

Solving all of the listed equation together, we find the harmonic amplitudes of the reflected field:

$$a_j = \frac{\varepsilon_{0j}\left(\Xi_j\frac{\varepsilon_1}{\gamma_{1j}} + \frac{4\pi\lambda_\omega}{\omega}b_0\right) - \frac{\Delta_{0j}}{\alpha_{0j}}}{b_0\left(\varepsilon_0 - \Xi_j\frac{\varepsilon_1 i\kappa_{0,j}}{\gamma_{1j}b_0} - \frac{4\pi\lambda_\omega}{\omega}i\kappa_{0,j}\right)} \tag{5}$$

Once amplitudes a_j are known, we can calculate the reflected electric field at any point in the region $z \geq 0$ using Eq. (3). Note that because $\varepsilon_{00} = \Delta_{00} = 0$, the expression is not singular for $j = 0$ and $a_j = 0$. For deriving the s-SNOM signal, we are interested in the scattered field magnitude E_0^{sc} at the tip center, where the effective dipole is located. This is linearly related to the dipole moment amplitude p_0:

$$E_0^{sc} = \beta p_0$$

where coefficient β can be calculated from Eqs. (1)–(3) and Eq. (5). Another equation giving the relation between the dipole polarization and the electric field acting on it is:

$$p_0 = \alpha E^{tot}, \alpha = \frac{a^2\varepsilon_0}{2}\frac{\varepsilon-\varepsilon_0}{\varepsilon+\varepsilon_0}$$

where ε is the dielectric permittivity of the tip's material and $E^{tot} = E_0 + E_0^{sc}$. Solving the equations above together, we find the relation between the dipole polarization and the incident wave amplitudes:

$$p_0 = \frac{\alpha E_0}{1-\alpha\beta}$$

The resulting s-SNOM signal is proportional to p_0. Note that for the simple case of a bare surface (when $\lambda_\omega = 0$) and almost isolated dipoles (when $d \gg h$), the relation between E_0^{sc} and p_0 is the following:

$$E_0^{sc} = \frac{\varepsilon_1-\varepsilon_0}{\varepsilon_0\left(\varepsilon_1+\varepsilon_0\right)}\frac{p_0^2}{2h^2}$$

Putting recent equations together and assume that the tip is perfectly conducting ($\varepsilon = -\infty$) we obtain the dipole moment *per unit length*:

$$p_0 = \frac{\varepsilon_0 a^2 / 2}{1 - \frac{\varepsilon_1 - \varepsilon_0}{(\varepsilon_1 + \varepsilon_0)} \frac{a^2}{4h^2}} E_0 \tag{6}$$

that is very similar to the formula obtained in the framework of the point dipole analysis [27]:

$$p_0' = \frac{\varepsilon_0 a^3}{1 - \frac{\varepsilon_1 - \varepsilon_0}{(\varepsilon_1 + \varepsilon_0)} \frac{a^3}{4h^3}} E_0 \tag{7}$$

where a is radius of spherical tip, h is the height of its center above the surface and p_0' is complex amplitude of oscillations of the *dipole moment*.

Assuming that the distance between the tip and the surface oscillates as

$$z(t) = \frac{z_{\min} + z_{\max}}{2} + \frac{z_{\min} - z_{\max}}{2} \cos \Omega t$$

where $z_{\min}$ = 5 nm and $z_{\max}$ = 50 nm are its minimum and maximum and Ω is the frequency of the mechanical oscillations, we can calculate the resulting s-SNOM signal $p_0(t)$ (in arbitrary units) in the time domain. Shifting the signal along the t-axis to make it symmetric, the value S_n is obtained as

$$S_n = \frac{\Omega}{\pi} \int_{-\frac{\pi}{\Omega}}^{\frac{\pi}{\Omega}} p_0(t) \cos n\Omega t \mathrm{d}t$$

according to [27].

Finalizing, we compare the S_2 signal from the bare InAs surface using the described model (cylindrical tip) with the signal in which we assumed that the tip is spherical [27] to determine whether or not they give the same results. Fig. 6 shows that the simulated signals, which are normalized to the corresponding reference signals from the gold surface, are very close to each other.

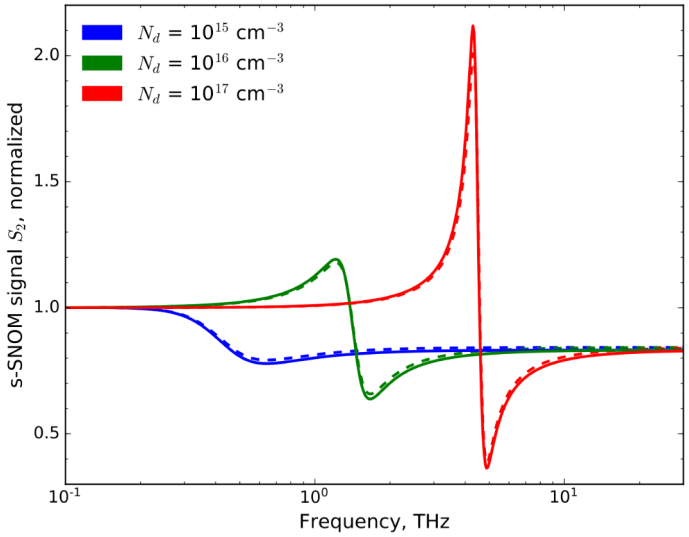

Fig. 6. Solid lines: frequency dependence of the S_2 signal from the InAs surface calculated for different doping levels N_d using Eq. (5) for the E-field reflectance, normalized to the S_2 signal the signals from InAs and from gold are calculated using the Eq. (7) for the E-field reflection.

The radius of the cylindrical or spherical tip is taken to be a = 30 nm. The dielectric permittivity of InAs and gold are modeled by the Drude formula with the parameters stated in the main text.

We conclude that in the case of a surface covered by 2d-materials, the described model with a cylindrical tip must give the result that is close to the model with the spherical one. However, the direct proof of this claim is quite difficult because of the significant bulkiness of the mathematical problem which considers a spherical s-SNOM tip above the investigated 2d-material and/or multilayered wafer.

Funding

National Science Foundation (NSF) (DMR 1508603, ECCS 1810252, DMR 1808491); Multidisciplinary University Research Initiative from the Air Force Office of Scientific Research (AFOSR MURI) (FA9550-12-1- 0488).

References

1. H.-T. Chen, R. Kersting, and G. C. Cho, "Terahertz imaging with nanometer resolution," Appl. Phys. Lett. **83**(15), 3009–3011 (2003).
2. K. Wang, D. M. Mittleman, N. C. J. Van Der Valk, and P. C. M. Planken, "Antenna effects in terahertz apertureless near-field optical microscopy," Appl. Phys. Lett. **85**(14), 2715–2717 (2004).
3. H.-G. von Ribbeck, M. Brehm, D. W. van der Weide, S. Winnerl, O. Drachenko, M. Helm, and F. Keilmann, "Spectroscopic THz near-field microscope," Opt. Express **16**(5), 3430–3438 (2008).
4. A. J. Huber, F. Keilmann, J. Wittborn, J. Aizpurua, and R. Hillenbrand, "Terahertz near-field nanoscopy of mobile carriers in single semiconductor nanodevices," Nano Lett. **8**(11), 3766–3770 (2008).
5. M. C. Giordano, S. Mastel, C. Liewald, L. L. Columbo, M. Brambilla, L. Viti, A. Politano, K. Zhang, L. Li, A. G. Davies, E. H. Linfield, R. Hillenbrand, F. Keilmann, G. Scamarcio, and M. S. Vitiello, "Phase-resolved terahertz self-detection near-field microscopy," Opt. Express **26**(14), 18423–18435 (2018).
6. H. T. Stinson, A. Sternbach, O. Najera, R. Jing, A. S. Mcleod, T. V. Slusar, A. Mueller, L. Anderegg, H. T. Kim, M. Rozenberg, and D. N. Basov, "Imaging the nanoscale phase separation in vanadium dioxide thin films at terahertz frequencies," Nat. Commun. **9**(1), 3604 (2018).
7. P. Klarskov, A. Pizzuto, and D. M. Mittleman, "Imaging on the nanoscale with THz time-domain, emission and pump-probe microscopy," in *2018 43rd International Conference on Infrared, Millimeter, and Terahertz Waves (IRMMW-THz)* (IEEE, 2018), pp. 1–2.
8. M. Eisele, T. L. Cocker, M. A. Huber, M. Plankl, L. Viti, D. Ercolani, L. Sorba, M. S. Vitiello, and R. Huber, "Ultrafast multi-terahertz nano-spectroscopy with sub-cycle temporal resolution," Nat. Photonics **8**(11), 841–845 (2014).
9. P. Klarskov, H. Kim, V. L. Colvin, and D. M. Mittleman, "Nanoscale laser terahertz emission microscopy," ACS Photonics **4**(11), 2676–2680 (2017).
10. T. Kampfrath, M. Battiato, P. Maldonado, G. Eilers, J. Nötzold, S. Mährlein, V. Zbarsky, F. Freimuth, Y. Mokrousov, S. Blügel, M. Wolf, I. Radu, P. M. Oppeneer, and M. Münzenberg, "Terahertz spin current pulses controlled by magnetic heterostructures," Nat. Nanotechnol. **8**(4), 256–260 (2013).
11. C. Zhou, Y. P. Liu, Z. Wang, S. J. Ma, M. W. Jia, R. Q. Wu, L. Zhou, W. Zhang, M. K. Liu, Y. Z. Wu, and J. Qi, "Broadband terahertz generation via the interface inverse Rashba-Edelstein effect," Phys. Rev. Lett. **121**(8), 086801 (2018).
12. M. B. Jungfleisch, Q. Zhang, W. Zhang, J. E. Pearson, R. D. Schaller, H. Wen, and A. Hoffmann, "Control of terahertz emission by ultrafast spin-charge current conversion at Rashba interfaces," Phys. Rev. Lett. **120**(20), 207207 (2018).
13. J. Nishitani, K. Kozuki, T. Nagashima, and M. Hangyo, "Terahertz radiation from coherent antiferromagnetic magnons excited by femtosecond laser pulses," Appl. Phys. Lett. **96**(22), 221906 (2010).
14. M. B. Jungfleisch, W. Zhang, and A. Hoffmann, "Perspectives of antiferromagnetic spintronics," Phys. Lett. A **382**(13), 865–871 (2018).
15. M. B. Lundeberg, Y. Gao, R. Asgari, C. Tan, B. Van Duppen, M. Autore, P. Alonso-González, A. Woessner, K. Watanabe, T. Taniguchi, R. Hillenbrand, J. Hone, M. Polini, and F. H. L. Koppens, "Tuning quantum nonlocal effects in graphene plasmonics," Science **357**(6347), 187–191 (2017).
16. J. Zhang, X. Chen, S. Mills, T. Ciavatti, Z. Yao, R. Mescall, H. Hu, V. Semenenko, Z. Fei, H. Li, V. Perebeinos, H. Tao, Q. Dai, X. Du, and M. Liu, "Terahertz nanoimaging of graphene," ACS Photonics **5**(7), 2645–2651 (2018).
17. G. X. Ni, A. S. McLeod, Z. Sun, L. Wang, L. Xiong, K. W. Post, S. S. Sunku, B. Y. Jiang, J. Hone, C. R. Dean, M. M. Fogler, and D. N. Basov, "Fundamental limits to graphene plasmonics," Nature **557**(7706), 530–533 (2018).
18. D. N. Basov, M. M. Fogler, A. Lanzara, F. Wang, and Y. Zhang, "Colloquium: graphene spectroscopy," Rev. Mod. Phys. **86**(3), 959–994 (2014).

19. Z. Fei, A. S. Rodin, G. O. Andreev, W. Bao, A. S. McLeod, M. Wagner, L. M. Zhang, Z. Zhao, M. Thiemens, G. Dominguez, M. M. Fogler, A. H. Castro Neto, C. N. Lau, F. Keilmann, and D. N. Basov, "Gate-tuning of graphene plasmons revealed by infrared nano-imaging," Nature **487**(7405), 82–85 (2012).
20. Z. Shi, C. Jin, W. Yang, L. Ju, J. Horng, X. Lu, H. A. Bechtel, M. C. Martin, D. Fu, J. Wu, K. Watanabe, T. Taniguchi, Y. Zhang, X. Bai, E. Wang, G. Zhang, and F. Wang, "Gate-dependent pseudospin mixing in graphene/boron nitride moiré superlattices," Nat. Phys. **10**(10), 743–747 (2014).
21. G. X. Ni, H. Wang, J. S. Wu, Z. Fei, M. D. Goldflam, F. Keilmann, B. Özyilmaz, A. H. Castro Neto, X. M. Xie, M. M. Fogler, and D. N. Basov, "Plasmons in graphene moiré superlattices," Nat. Mater. **14**(12), 1217–1222 (2015).
22. S. S. Sunku, G. X. Ni, B. Y. Jiang, H. Yoo, A. Sternbach, A. S. McLeod, T. Stauber, L. Xiong, T. Taniguchi, K. Watanabe, P. Kim, M. M. Fogler, and D. N. Basov, "Photonic crystals for nano-light in moiré graphene superlattices," Science **362**(6419), 1153–1156 (2018).
23. H. R. Seren, J. Zhang, G. R. Keiser, S. J. Maddox, X. Zhao, K. Fan, S. R. Bank, X. Zhang, and R. D. Averitt, "Nonlinear terahertz devices utilizing semiconducting plasmonic metamaterials," Light Sci. Appl. **5**(5), e16078 (2016).
24. S. N. Gilbert Corder, X. Chen, S. Zhang, F. Hu, J. Zhang, Y. Luan, J. A. Logan, T. Ciavatti, H. A. Bechtel, M. C. Martin, M. Aronson, H. S. Suzuki, S. I. Kimura, T. Iizuka, Z. Fei, K. Imura, N. K. Sato, T. H. Tao, and M. Liu, "Near-field spectroscopic investigation of dual-band heavy fermion metamaterials," Nat. Commun. **8**(1), 2262 (2017).
25. S. N. Gilbert Corder, J. Jiang, X. Chen, S. Kittiwatanakul, I.-C. Tung, Y. Zhu, J. Zhang, H. A. Bechtel, M. C. Martin, G. L. Carr, J. Lu, S. A. Wolf, H. Wen, T. H. Tao, and M. Liu, "Controlling phase separation in vanadium dioxide thin films via substrate engineering," Phys. Rev. B **96**(16), 161110 (2017).
26. N. F. Hartmann, T. Gokus, M. Eisele, and A. J. Huber, "Conductivity mapping in graphene through scattering-type scanning near-field optical microscopy in the mid-infrared and terahertz spectral region with 25nm spatial resolution," in *Electrochemical Society Meeting* (The Electrochemical Society, 2018), **MA2018-01**(10), p. 872.
27. R. Hillenbrand, B. Knoll, and F. Keilmann, "Pure optical contrast in scattering-type scanning near-field microscopy," J. Microsc. **202**, 77–83 (2001).
28. G. W. Hanson, "Dyadic Green's functions and guided surface waves for a surface conductivity model of graphene," J. Appl. Phys. **103**(6), 064302 (2008).
29. R. Jacob, S. Winnerl, H. Schneider, M. Helm, M. T. Wenzel, H.-G. von Ribbeck, L. M. Eng, and S. C. Kehr, "Quantitative determination of the charge carrier concentration of ion implanted silicon by IR-near-field spectroscopy," Opt. Express **18**(25), 26206–26213 (2010).
30. T. Taubner, R. Hillenbrand, and F. Keilmann, "Performance of visible and mid-infrared scattering-type near-field optical microscopes," J. Microsc. **210**, 311–314 (2003).
31. A. J. Huber, D. Kazantsev, F. Keilmann, J. Wittborn, and R. Hillenbrand, "Simultaneous IR material recognition and conductivity mapping by nanoscale near-field microscopy," Adv. Mater. **19**(17), 2209–2212 (2007).
32. J. B. Héroux and M. Kuwata-Gonokami, "Photoexcited carrier dynamics in InAs, GaAs, and InSb probed by terahertz excitation spectroscopy," Phys. Rev. Appl. **7**(5), 054001 (2017).
33. E. D. Palik, *Handbook of Optical Constants of Solids* (Academic Press, 2012).
34. L. F. J. Piper, T. D. Veal, M. J. Lowe, and C. F. McConville, "Electron depletion at InAs free surfaces: Doping-induced acceptor like gap states," Phys. Rev. B Condens. Matter Mater. Phys. **73**(19), 195321 (2006).
35. R. L. Olmon, B. Slovick, T. W. Johnson, D. Shelton, S. H. Oh, G. D. Boreman, and M. B. Raschke, "Optical dielectric function of gold," Phys. Rev. B Condens. Matter Mater. Phys. **86**(23), 235147 (2012).
36. J. L. Garcia-Pomar, A. Y. Nikitin, and L. Martin-Moreno, "Scattering of graphene plasmons by defects in the graphene sheet," ACS Nano **7**(6), 4988–4994 (2013).
37. L. Jiang, Z. Shi, B. Zeng, S. Wang, J.-H. Kang, T. Joshi, C. Jin, L. Ju, J. Kim, T. Lyu, Y.-R. Shen, M. Crommie, H.-J. Gao, and F. Wang, "Soliton-dependent plasmon reflection at bilayer graphene domain walls," Nat. Mater. **15**(8), 840–844 (2016).
38. E. J. Nicol and J. P. Carbotte, "Optical conductivity of bilayer graphene with and without an asymmetry gap," Phys. Rev. B Condens. Matter Mater. Phys. **77**(15), 155409 (2008).
39. M. Jablan, H. Buljan, and M. Soljačić, "Transverse electric plasmons in bilayer graphene," Opt. Express **19**(12), 11236–11241 (2011).